Structural, microstructural and multiferroic properties of $BiFeO_3$–$CoFe_2O_4$ composites

Samiksha Dabas[1] · Prachi Chaudhary[1] · Manish Kumar[2] · S. Shankar[1,2] · O. P. Thakur[1]

Abstract

$BiFeO_3$–$CoFe_2O_4$ composites were successfully prepared via conventional solid state method. Powder X-ray diffraction confirmed the presence of both perovskite $BiFeO_3$ (BFO) and spinel $CoFe_2O_4$ (CFO) phases and rhombohedral structure due to splitting in major peaks in the composites. Further insight into the microstructural and morphological properties of the composites was provided by Raman spectra, Fourier Transform Infrared Spectroscopy and Field Emission Scanning Electron Microscopy along with EDX analysis. Magnetic and electrical response of the composites has been studied exhaustively to comprehend their multiferroic properties. Magnetization study (magnetization vs. magnetic field) confirmed the high saturation magnetization in composites with a low value of coercivity at room temperature. The maximum saturation magnetization (0.3902 emu/g) was achieved in BFO–30%CFO. Ferroelectric polarization (polarization vs. electric field) loop measurements confirmed the low electrical leakage current in the composites. The temperature dependent dielectric response of the composites suggested existence of magnetoelectric coupling between the ferroelectric and ferromagnetic orders in the vicinity of antiferromagnetic–paramagnetic transition temperature of BFO. The decrease in dielectric loss with an increase in CFO content in the composites also validated the similar results as observed in polarization versus electric field measurements. The Impedance Spectroscopy at room temperature revealed the non-Debye behavior and high resistivity of the composites.

1 Introduction

Lead free multiferroics such as Bismuth Ferrite due to their overarching potential have revitalized the attention of researchers in the fabrication of novel device applications employing the concept of ME coupling such as MEMS, spintronics, piezo-electric sensors, field-controlled ferromagnetic resonance, transducers, non-volatile memory elements, etc. Apart from the multiferroism, numerous intriguing physical phenomena occur due to the well-built coupling between ferroelectric and magnetic order parameters, i.e., magnetoelectric coupling [1]. Ferroelectricity and ferromagnetism are generally mutually exclusive, ferromagnetism

requires partially and ferroelectricity require empty or completely filled transition metal orbital ('d' orbital). So, only few multiferroic materials exist in the nature.

Magnetoelectric (ME) properties of $BiFeO_3$ (BFO) with a rhombohedrally distorted perovskite structure of type ABO_3 and single-phased multiferroic, are attributed to its ferroelectric and weak antiferromagnetic orders. Ferroelectricity in BFO is ascribed to the lone pair mechanism; stereochemically active pairs of valence electrons at A-site cations in 6 s orbital of Bi^{3+} which instead of undergoing sp hybridization, create a local dipole. This results in spontaneous polarization of ~ 100 μCcm^{-2} along [111] axis in rhombohedral unit cell, consistent with space group R3c, below Curie temperature ($T_c = 873$ °C) [2]. The unpaired d^5 electron configuration of Fe^{3+} ions in BFO gives rise to a weak G-type antiferromagnetic ordering which exists below Neel temperature ($T_N = 370$ °C) [3–5]. Dzyaloshinskii–Moriya interaction or asymmetric exchange arises due to the tilting of Oxygen octahedron which surrounds Fe^{3+} ion to form a close packing thereby producing a small canting (Fe–O–Fe angle). This induces a weak local magnetization which is averaged out to zero due to the existence of spin cycloid structure (period ~ 620 Å). But the macroscopic canting of antiferromagnetic

✉ Manish Kumar
  manishphy2007@gmail.com

✉ O. P. Thakur
  opthakur@yahoo.com

1 Materials Analysis & Research Laboratory, Department of Physics, NSUT, New Delhi 110078, India

2 Experimental Research Laboratory, Department of Physics, ARSD College, University of Delhi, New Delhi 110021, India

moments still exists at localized unit cell level which can be recovered in presence of high magnetic fields i.e., magnetic field greater than critical field (spin cycloid gets destroyed) [6, 7]. A quadratic ME coupling is observed [8, 9] at a field below the critical magnetic field. There exist few processing issues such as loss of Bi at the time of reaction which effectuates BFO to show semiconducting nature near room temperature and high dielectric loss [10]. Low resistivity, high dielectric loss, high leakage current, weak ME coupling of BFO pose a hindrance for its practical applications. Various attempts have been made by researchers worldwide to overcome these inherent limitations by fabricating BFO based nanocomposites heterostructures, BFO-based solid solutions, etc.

Potential applications of BFO as a microwave attenuation material have been successfully studied by researchers. Enhancement of magnetic loss and henceforth a matching between the dielectric loss and magnetic loss for improvement in its electromagnetic properties can be achieved by doping BFO with suitable materials or by BFO based composites [11, 12]. In comparison with bulk, enhanced magnetization of BFO nanoparticles is observed which indicates a dependence of particle size on magnetic properties. This dependence is attributed to anisotropic stresses and decompensates spins on nanoparticles surface in addition to frustration of antiferromagnetism [13]. Recently, it is found that with decrease in particle size, the ME coupling exhibits a non monotonic variation due to the enhanced lattice strain and compressive pressure in the nanoparticles of BFO [14]. ME coupling is observed in BFO based epitaxial thin films [15]. This suggests that the spiral spin structure which is responsible for inhibition of linear ME effect and also for cancellation of macroscopic magnetization can be suppressed. However, problems of reduction in leakage current density and coercivity still persist in the BFO-based thin films. Enhanced multiferroic properties have been explored by researchers successfully [16, 17] by substitution of transition metal ions, alkaline rare earth metal ions, lanthanides at Bi-site and transition metal ions at Fe-site. Highest spontaneous magnetization is observed in case of substitution of rare earth metal ions. Enhanced strain-mediated ME effect is observed in the form of increased piezo response with application of magnetic field in BFO–CFO nanocomposite heterostructures overcoming clamping effect and reducing leakage current as reported by Li et al. [18]. Desirable ME effect can be obtained via suitable combination of piezoelectric and piezomagnetic or magnetostrictive phases. Such composites have applications in many multifunctional devices such as—memory devices based on ME effect.

The magnetic spinel ferrites like $CoFe_2O_4$ (CFO), belonging to space group Fd–3m, have attracted significant interest due to their outstanding electrical, dielectric, optical, mechanical, thermal and magnetic properties [19, 20].

Spinel ferrites structure is of type AB_2O_4 where A is a divalent metal ion occupying tetrahedral interstitial sites and B is a trivalent metal ion occupying octahedral interstitial sites. The distribution of the cations amongst the two interstitial sites of spinel lattice of CFO makes it very sensitive for the magnetic properties. Magnetic CFO is very useful under the cation distribution in the recent technology mainly on magnetic and magneto-optical recording media. Such applications of CFO are due to its important properties such as strong anisotropy, high saturation magnetization and coercivity along with good mechanical hardness and chemical stability [21].

Magnetic properties of multiferroic BFO (also ME coupling) are weak as a consequence of cycloidal spin structure and consequently can be enhanced by incorporating CFO. CFO, a widely used ferromagnetic material is known for its high coercivity (~ 5400 Oe) and saturation magnetization (~ 80 emu/g), good chemical stability, large magnetostrictive coefficient [22]. Also, in order to observe hysteresis loop and enhanced resistivity of the bulk BFO, there is a need of modification and preparation of the BFO with other suitable materials. As per the literature, BFO is antiferromagnetic as well as ferroelectric; there is a need to enhance its magnetic properties. In this respect, CFO is a useful material for composite formation with BFO so as to get better multiferroic results for the numerous device applications in spintronics and sensor technologies. The multiferroic properties of BFO–CFO composites have been investigated in the literature [23–26], but more attention towards multiferroic properties is needed. So, in this paper, we have focused on the microstructural and multiferroic properties of perovskite-spinel (BFO–CFO) composites synthesized via solid state reaction technique.

2 Experimental

Pure BFO and CFO with other three composite samples (BFO–10%CFO, BFO–20%CFO and BFO–30%CFO) were synthesized via solid state reaction route using analytical reagents viz—Bi_2O_3, Fe_2O_3, CoO and Fe_2O_3 (purity ≥ 99.99%). Requisite stoichiometric amounts were weighed, ground thoroughly in an acetone medium till the acetone dried off completely. Mixture was then transferred into a crucible and calcined at 700 °C for 6 h. Polyvinyl acetate was added to the reaction mixture which acts as a binder for granulation. The ceramic mixture was then pressed into 1.0 cm diameter pellets in an automatic hydraulic press. Similarly spinel ferrite CFO was separately prepared by thoroughly mixing CoO and Fe_2O_3 calcined at 700 °C for 6 h. Finally, with requisite molar ratio of BFO–CFO (BFO–10%CFO, BFO–20%CFO and BFO–30%CFO), the ferrite composites were subsequently sintered at 820 °C for 9 h. Pure BFO,

CFO and composites of BFO–CFO pellets were sintered at 800 °C for 8 h.

Powder X-ray diffraction (XRD) patterns were recorded using Bruker D-8 advance X-ray diffractometer employing Cu–K$_\alpha$ radiations. Raman spectra were analysed using Renishaw Invia Reflux Micro Raman spectrometer. Fourier Transform Infrared Spectroscopy (FTIR) was performed using Perkin Elmer Fourier transform infrared spectrometer. FESEM micrographs with EDX analysis were reported using ZEISS Gemini SEM 500 field emission scanning scanning electron microscope. Room temperature study of magnetic hysteresis loop was done using a Vibrating Sample Magnetometer (Model: Micro Sense EV9) under a magnetic field of 10,000 Oe. Study of polarization vs electric field loop was performed employing 'Marine India' instrument operated at field of 5 kV/cm and at frequency 50 Hz. Temperature dependent dielectric study and impedance spectroscopy have been performed using Wayne Kerr 6500B Precision Impedance Analyzer in the frequency range of 1 Hz–1 MHz.

3 Results and discussion

Figure 1a shows the powder X-ray diffraction patterns of BFO, CFO and BFO–CFO composites. All peaks have been indexed using the standard JCPDS files for pure BFO, CFO and BFO–10%CFO, BFO–20%CFO and BFO–30%CFO composites. The pure phase of CFO has been confirmed from presence of peaks denoted by '#' at the corresponding diffraction angles. The CFO peaks become prominent with increasing content of CFO in the BFO–CFO composites. This shows presence of both phases i.e., CFO and BFO separately in the final composite. The diffraction peaks have been indexed on basis of hexagonal unit cell. The XRD patterns have shown the presence of CFO phase with BFO and have confirmed the composite formation for BFO–10%CFO, BFO–20%CFO and BFO–30%CFO samples. XRD patterns of all BFO–CFO composites exhibit splitting in the major 2θ (near 31.765°) peak and indicates a rhombohedral structure as depicted in Fig. 1b [27]. There is an impurity peak of Bi$_2$Fe$_4$O$_9$ in the composites that occur near 27.68° indicated by '*'.

Lattice dynamics of BFO–CFO composite were measured via Raman scattering. Changes in Raman mode have been attributed to the magnetostrictive stress of CFO layer that gets mechanically transferred to the BFO layer [28]. The optic phonons corresponding to the R3c structure are [29]

$$\Gamma_{R3c} = 4A_1(z, x^2 + y^2, z^2) + 5A_2(-) + 9E(x, y, x^2 - y^2, xy, xz, yz).$$

Here, 4A$_1$ and 9E modes are Raman active while 5A$_2$ modes are silent. Phonons vanish from the Raman spectra above T$_C$. The lattice properties and structural phase transitions are demonstrated via Raman spectroscopy. The group
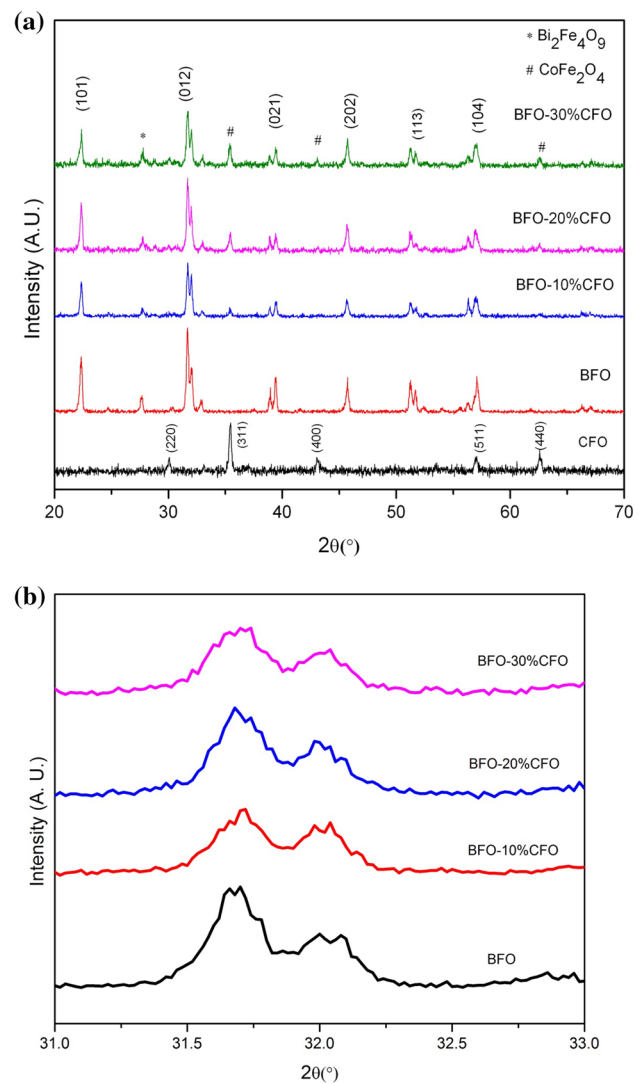
Fig. 1 **a** Room temperature powder XRD patterns of CFO, BFO, BFO–CFO composites prepared via solid state reaction technique. **b** Enlarged view of BFO and BFO–CFO composites showing peak splitting thereby conforming rhombohedral structure of BFO and its composites
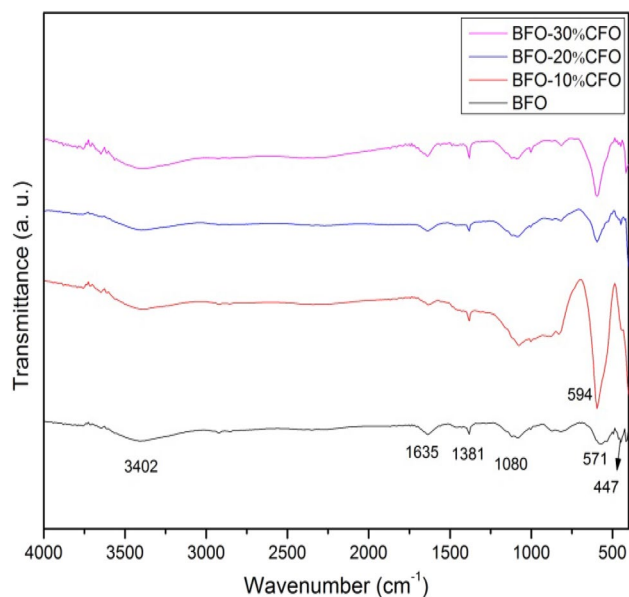
theory predicts 13 optical modes for rhombohedrally distorted structure (space group R3c)-BFO: r$_{Raman}$ = 4A$_1$ + 9E [30] where A$_1$ (transverse optical) and E (longitudinal optical components) modes are Raman active. To confirm the coexistence of both BFO and CFO phase in the BFO–CFO composite, the Raman spectra were measured as shown in Fig. 2. The well defined five Raman peaks for CFO—197, 294, 464, 600 and 684 cm^{-1}—have been identified as optical active Raman modes namely, A$_g$, E$_g$, 3F$_{2g}$. The modes—600 and 684 cm^{-1} correspond to the stretching vibration of FeO$_4$ tetrahedral sub lattice whereas the modes—197, 294 and 464 cm^{-1} depict the oxygen bending towards metal in O-site octahedral sub lattice. For BFO phase 4A$_1$ and
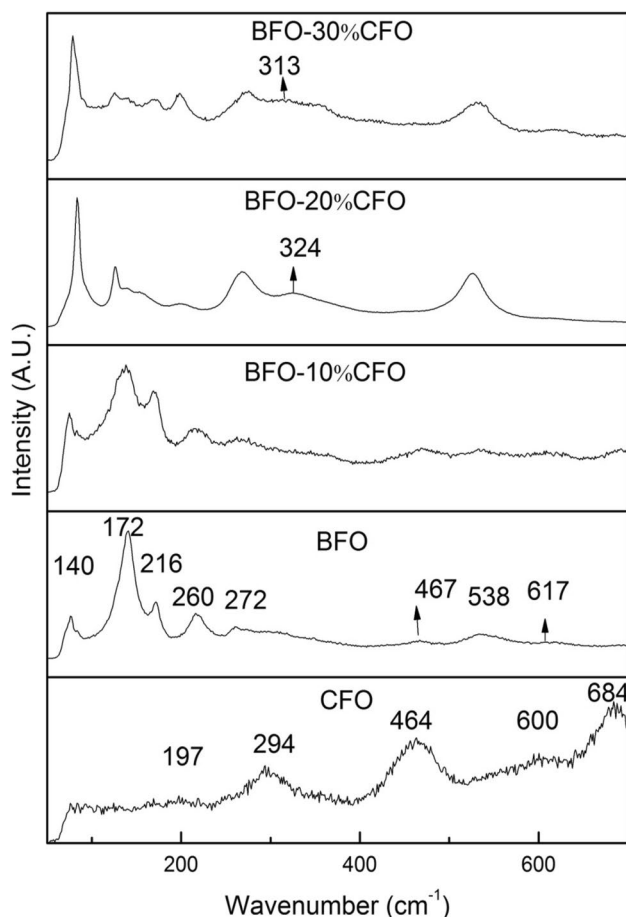
Fig. 2 Raman spectra of CFO, BFO, BFO–CFO composites

Fig. 3 Fourier Transform Infrared Spectroscopy (FTIR) of BFO and BFO–CFO composites

4E modes are observed at—140, 172, 216, 260, 272, 467, 538 and 617 cm^{-1}. The peaks at smaller wave number side (less than 300 cm^{-1}) correspond to Bi–O vibration while those at higher wavenumber side are associated with Fe–O vibrations. Since the BFO–CFO composite consists of two phases i.e., BFO and CFO, the observed Raman spectra for composites contain the Raman modes corresponding to pure BFO and CFO phases separately or it may also be due to the grain boundary region between the two respective phases. This explains the existence of some strange Raman peaks in the composite besides the BFO and CFO phases, 324 cm^{-1} in BFO–20%CFO and 313 cm^{-1} in BFO–30%CFO.

Figure 3 shows the transmittance spectra of BFO–CFO composites in wave number range of 400–4000 cm^{-1}. Chemical and molecular structural changes in composite can be understood with help of FTIR spectra. The vibration band appearing in BFO–CFO composites at 594 cm^{-1} corresponds to the metal–oxygen stretching mode vibrations associated with Fe–O or Co–O in CoFe$_2$O$_4$. The absorption bands for BFO have been observed at—3402, 1635, 1381, 1080, 571, 447 cm^{-1}. The absorption bands present between 400 and 700 cm^{-1} correspond to Fe–O vibrations.

Absorption bands around 571 and 471 cm^{-1} are ascribed to stretching and bending mode vibrations respectively. The broadening of absorption band around 571 cm^{-1} has indicated overlapping of wave numbers associated with Fe–O and Bi–O vibrations [31]. The absorption band at 3402 cm^{-1} and 1635 cm^{-1} are ascribed to O–H stretching and H–O–H bending vibration modes respectively whose presence indicates that the composite gained moisture.

The field emission scanning electron microscopy (FESEM) micrographs recorded in the 1–2 μm range in the composite have been shown in Fig. 4. The agglomeration of BFO in the composites as observed was due to the different processing temperatures of Fe and Bi as a result of which Bi may be melted. The composites exhibited compact and heterogeneous microstructures crystallized into separate phases due to the significant difference in the sintering temperature and the thermal expansion coefficient of the two phases in the composites i.e., BFO and CFO. Some of the grains, due to their higher growth probability, grow at expense of others inhibiting the latter's growth. Larger grain sizes are attributed to the oxygen vacancies and result in decrease in stress at the grain boundaries. As a result, we observed the ferroelectric hysteresis loops. Also, the larger grain sizes are associated with dominant effects of incommensurate cycloidal spin structure in pure BFO which is responsible for a very low magnetization. Magnetization improves only with incorporation of magnetic phase i.e., CFO to form BFO–CFO composites. The EDX analysis, depicted in Fig. 4 confirms the exact amount of BFO and CFO in the composites. All
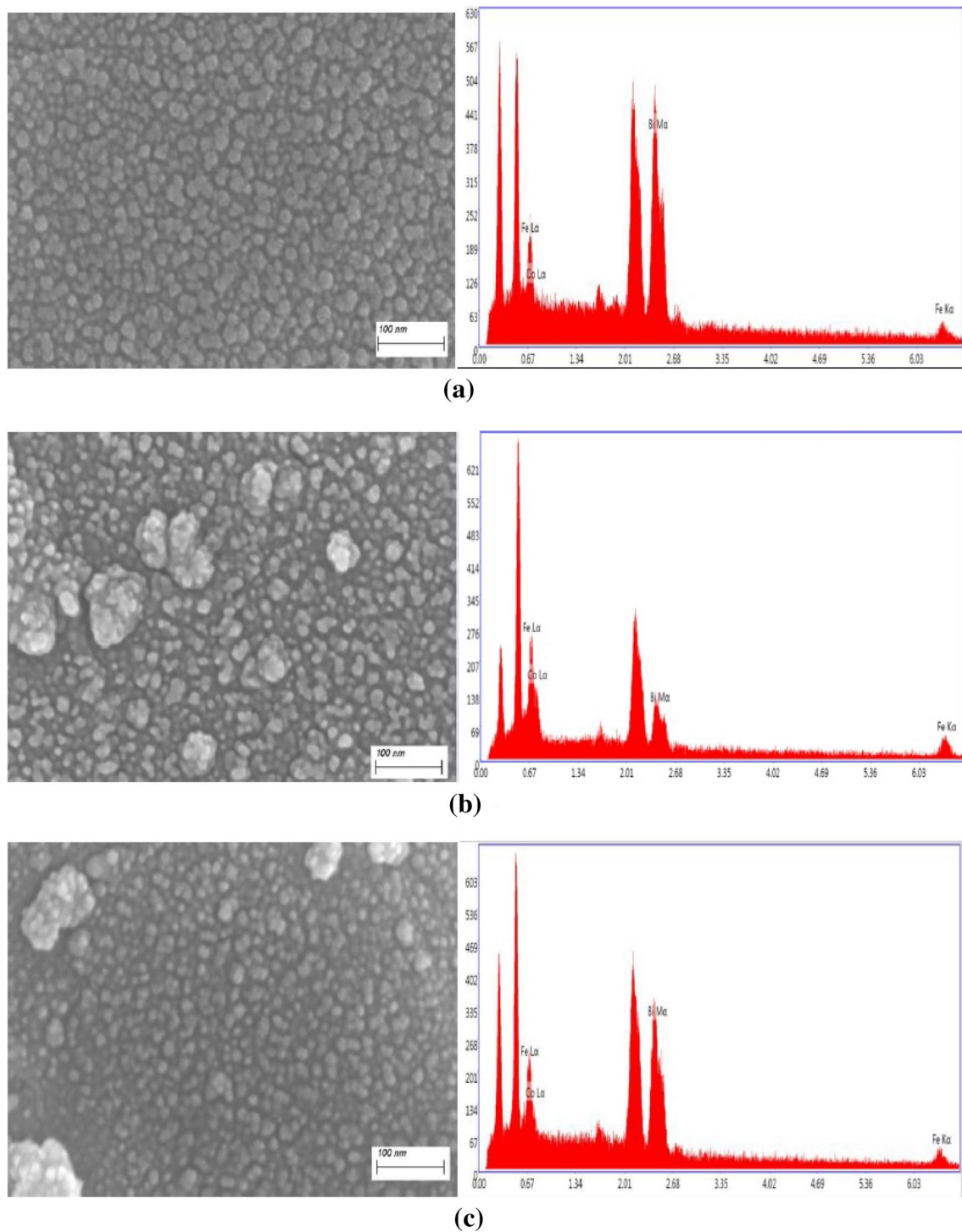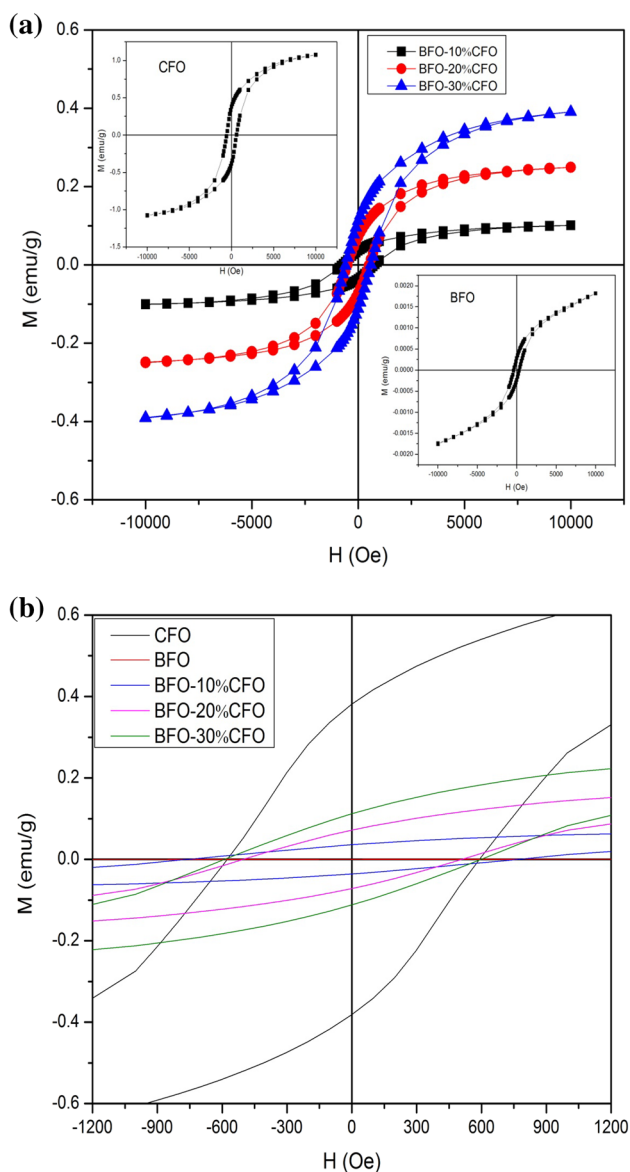
Fig. 4 FESEM micrographs with EDX analysis for **a** BFO–10%CFO, **b** BFO–20%CFO and **c** BFO–30%CFO composites in the range 1–2 μm depicting heterogeneous microstructures

the EDX images show the presence of Bi, Co and Fe in the composites.

Room temperature magnetization of the BFO–CFO composites samples has been measured using the vibrating sample magnetometer at an applied magnetic field of 10,000 Oe. Figure 5a shows the M versus H hysteresis loops of BFO–10%CFO, BFO–20%CFO and BFO–30%CFO composites and insets of Fig. 5a shows the hysteresis loops of pure BFO and CFO samples. The magnetization of the composite samples increases rapidly at low fields and tends to

Table 1 Variation of coercivity, saturation magnetization and remanent magnetization at field of 10,000 Oe near room temperature

Sample	H_c (Oe)	M_s (emu/g)	M_r (emu/g)
BFO–10%CFO	740	0.1012	0.0352
BFO–20%CFO	540	0.2474	0.0720
BFO–30%CFO	560	0.3902	0.1088

of Fe^{3+} ions at octahedral sites [32, 33]. Figure 5b shows the enlarged view of the hysteresis loops and also confirm the coercivity values in the composites in comparison with BFO.

Figure 6 depicts the room temperature electric hysteresis loops (P vs. E) of pure BFO and BFO–CFO composites were measured at frequency of 50 kHz with an applied electric field of 5 kV/cm. The maximum ferroelectric polarization of pure BFO, BFO–10%CFO, BFO–20%CFO and BFO–30%CFO composite samples was found to be 9.6, 8.2, 5.1 and 3.1 μCcm^{-2} respectively measured along the diagonals of the perovskite unit cell $(111)_{pseudocubic}/(001)_{hexagonal}$ [34]. However saturation polarization could not be achieved in any of the composites due to the rounded corners of the hysteresis loops. The P versus E loops depict that the area under the loop, representative of the loss in the material samples, decreases significantly on increasing the magnetic CFO content in to BFO in the composites. Low lossy ceramics because of their reduced leakage current and improved electrical properties can be used in the memory devices and spintronics technology applications.

Fig. 5 **a** Room temperature M–H curve for BFO–CFO composites. Inset shows M–H curve of pure BFO and CFO. **b** Enlarged view of room temperature M–H curve shows the stable, consistent and low coercivity values of BFO–CFO composites
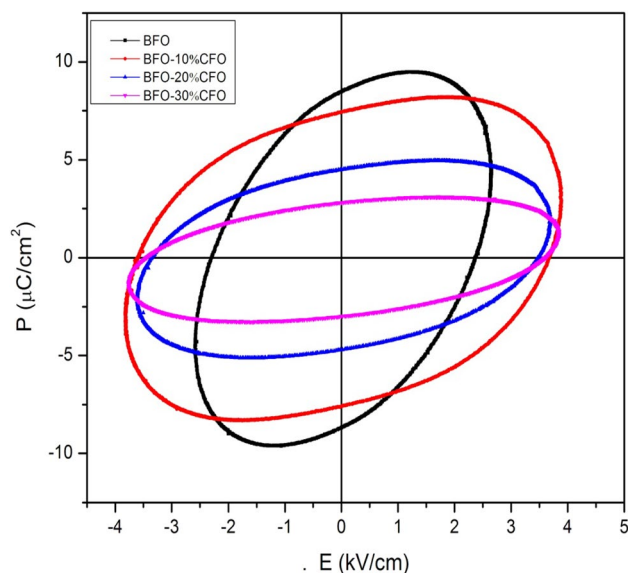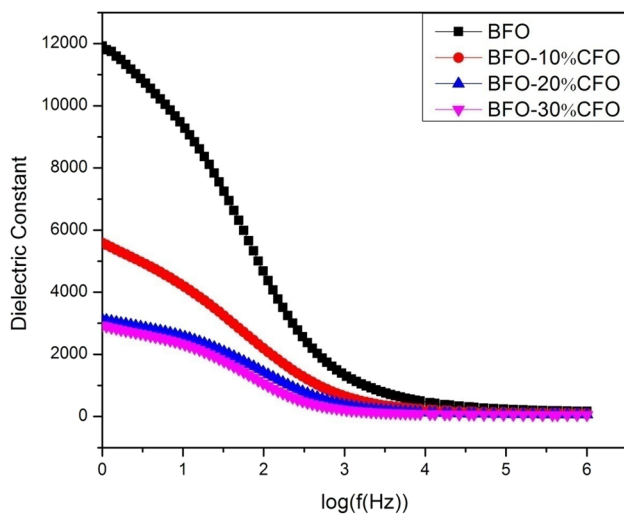
saturate at higher fields. Pure BFO shows the almost antiferromagnetic hysteresis loop but when we increase the magnetic constituent of the composite saturation magnetization achieved with low value of coercivity which is useful in the memory devices as well as spintronics applications. In the same way, the saturation magnetization as well as remnant magnetization also increases with the increase of CFO content in to BFO as also shown in Table 1. The reason of the enhancement in magnetization properties of BFO after the addition of CFO is due to the canted antiferromagnetic order of Fe–O–Fe chain spins resulting in a weak spontaneous magnetic moment and also due to the statistical distribution

Fig. 6 Room temperature ferroelectric loop (P–E curve) for BFO and BFO–CFO composites

**Fig. 7** Room temperature variation of dielectric constant with frequency for BFO and BFO–CFO composites

Room temperature plot dielectric constant as a function of frequency in the frequency range 1 Hz–1 MHz is depicted in Fig. 7. All composites exhibit a decreasing nature of dielectric constant with increased frequency displaying low-frequency region dispersion. This decrease is attributed to space charge polarization arising because of multiple vacancies of Fe ions in ferrite phase, vacancies at A-site and oxygen vacancies [35]. The decrease in dielectric constant with frequency is the usual Maxwell–Wagner type interfacial polarization for dipolar relaxation in agreement with Koop's phenomenological theory. Unlike in high frequency region, at low frequencies the dipoles are able to follow the applied field and therefore have high value of the dielectric constant [36]. Upon increasing the content of CFO in BFO composite, there is a tremendous decrease observed in dielectric constant. This could possibly be due to the suppression of ferroelectric order in BFO due to the superparamagnetic phase of CFO. In composites, the multiphase interface effects of interfacial polarization and heterogeneous conduction is inevitable and becomes significant in case of high ferrite content. In the composites, high dielectric constant value observed at low frequencies is attributed to the heterogeneous conduction [37] and polaron hopping mechanism leading to electronic polarization thereby contributing to low frequency dispersion of dielectric constant [38]. Dielectric behaviour can also be explained by polarization mechanism because CFO, a piezomagnetic material, is responsible for conduction beyond phase percolation limits. Net polarization is observed due to the local displacement of p-type carriers viz—Bi^{2+}/Bi^{3+} and Co^{2+}/Co^{3+} in the presence of external electric field in addition to that of n-type carriers. However, the n-type carrier contribution due to electronic exchange between Fe^{3+} and Fe^{2+} ions is more than

the p-type contribution and also both are of opposite signs as the mobility of n-type carriers is more than p-type carriers. This causes the net polarization to decrease more rapidly and then gradually decrease with an increase in frequency.

Temperature dependence of dielectric parameters as a function of temperature at varying frequencies has been studied for BFO–CFO composites. Figure 8 depicts the position of the sharp dielectric peaks of composites at varying frequency 10 kHz and 100 kHz. Peak anomalies have been observed as evident from which gradually shift towards the lower temperature side with an increase in CFO content in the composite. The obtained dielectric behaviour can be explained on basis of dipolar and interfacial polarization at lower frequencies and electronic polarization at higher frequencies. The transition temperature of composites remains constant with varying frequencies. Reduction in dielectric constant with an increase in ferrite content is due to the incorporation of ferromagnetic phase in the dominant ferroelectric phase of BFO which henceforth dilutes the ferroelectric properties of the composites. The observed peak anomalies in the vicinity of the antiferromagnetic Neel temperature of BFO (643 K) indicate a magnetic transition and orientation of magnetic dipoles of BFO in presence of an external electric field [39, 40]. This suggested the existence of a ME coupling in the vicinity of antiferromagnetic to paramagnetic transition temperature in the composites [41]. The peak anomaly reduces with an increase in the CFO content in the composite. This has been attributed to the presence of a ferromagnetic
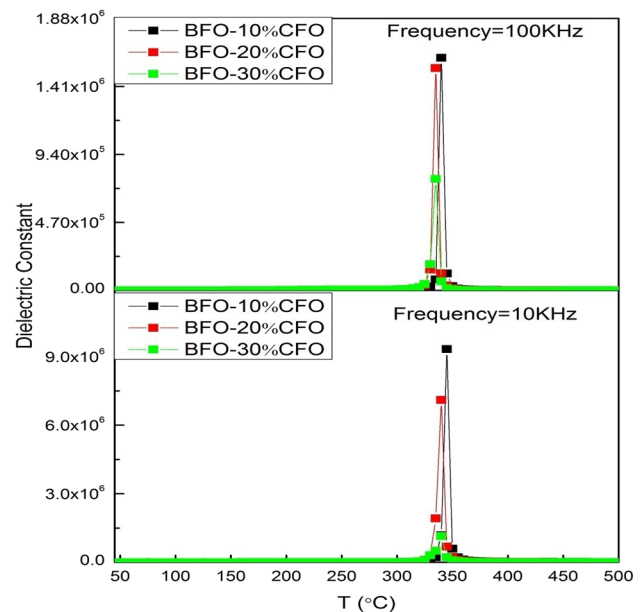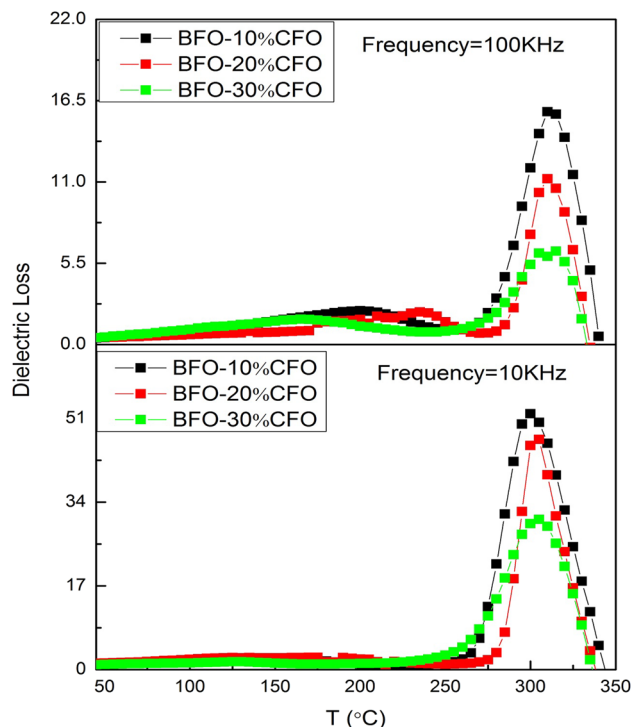

Fig. 8 Temperature dependence of dielectric constant i.e., real part (ε′) of permittivity for BFO–CFO composites at frequencies of 10 kHz and 100 kHz
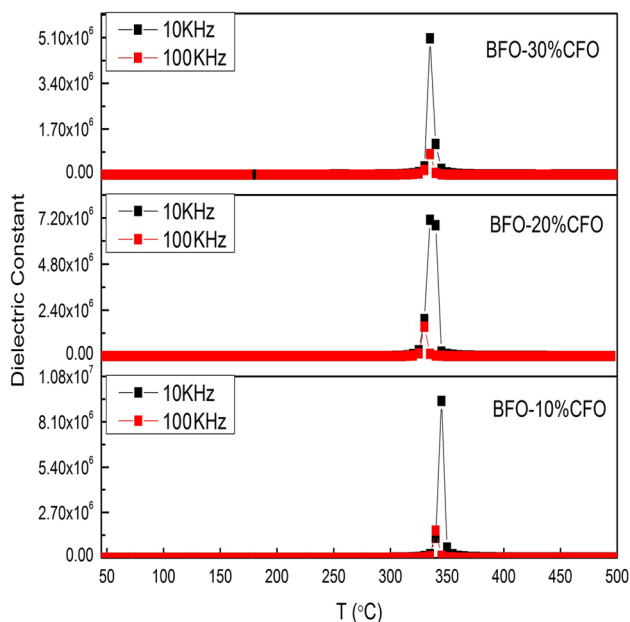
Fig. 9 Temperature dependence of dielectric constant i.e., real part (ε′) of permittivity at frequencies 10 kHz and 100 kHz for BFO–10%CFO, BFO–20%CFO and BFO–30%CFO

Fig. 10 Temperature dependence of dielectric loss i.e., imaginary part (ε″) of permittivity for BFO–CFO composites at 10 kHz and 100 kHz

phase of CFO which suppresses the antiferromagnetic phase of BFO. Also, dielectric constant decreases with an increase in applied frequency as evident from Fig. 9. This is because the various polarization contributions to the dielectric constant are unable to follow the rapidly oscillating applied electric field. As shown in Fig. 10, decrease in dielectric loss (tanδ) on increasing the CFO content in the composite is observed. Also, dielectric loss (tanδ) decreases with an increase in frequency as evident from Fig. 11. Nevertheless, the high dielectric loss in the composites is indicative of increase in charge carrier hopping of Fe^{3+}/Fe^{2+} ions.

Room temperature impedance spectroscopy analysis, a pivotal tool employed to study Z″ versus Z′ plot, is shown in Fig. 12. The Cole–Cole plot for pure BFO depicted a semicircle starting from origin and intercept on real axis with large radius thereby indicating the contribution due to grain effect only. However with the addition of CFO, the BFO–CFO composites display two arcs: first and second semicircle corresponding to grains and grain boundary contributions respectively. The non-Debye type behavior is observed in the Cole–Cole plots due to their centres of semicircles lie below the real axis. On addition of CFO, the radius of first semicircle is found to increase suggesting an increase in the grain resistance. However, the radius of second semicircle more or less remains the same. Nevertheless, we can conclude that the BFO–CFO composites are highly resistive.

4 Conclusions

Pure BFO, CFO and BFO–CFO composites have been prepared via solid state reaction route. The splitting of XRD peaks have confirmed the rhombohedral structure and composite formation with small amount of impurity ($Bi_2Fe_4O_9$). Ferroelectric polarization analysis confirmed the low loss in the composite samples which has also been validated by the decrease in dielectric loss with an incorporation of magnetic phase (CFO) in the composites. The low loss in the composites is useful for spintronics and memory device applications. The dielectric dispersion with frequency has been interpreted on basis of heterogeneous conduction and polaron hopping mechanism. Temperature dependent dielectric behaviour has been explained on basis of dipolar and interfacial polarization at lower frequencies and electronic polarization at higher frequencies. Peak anomaly in the vicinity of antiferromagnetic–paramagnetic transition indicates magnetoelectric coupling in composites. Impedance analysis confirmed the non-Debye type behavior and highly resistive samples. In conclusion, our results stipulate the microstructural properties, low dielectric loss, energy storage device applications and ME coupling in BFO–CFO ceramics.
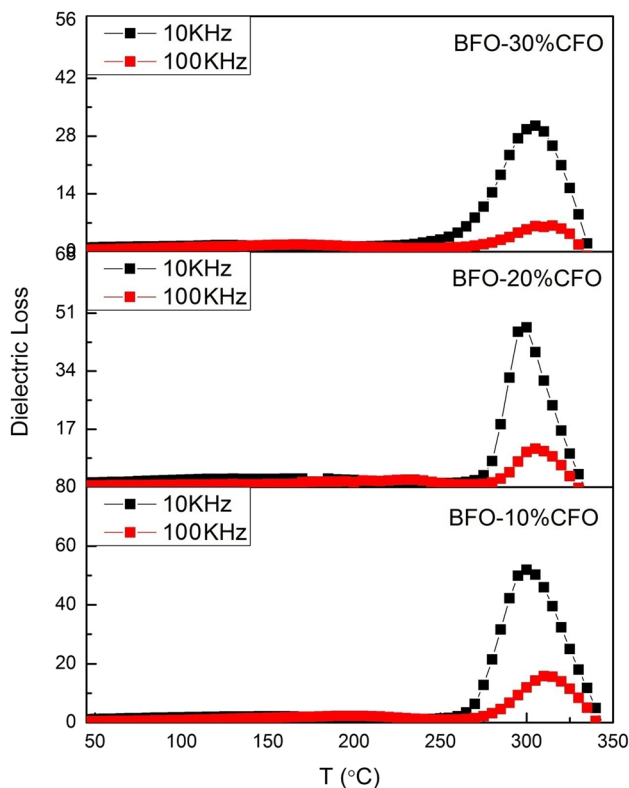
Fig. 11 Temperature dependence of dielectric loss i.e., imaginary part (ε'') of permittivity at frequencies 10 kHz and 100 kHz for BFO–10%CFO, BFO–20%CFO and BFO–30%CFO
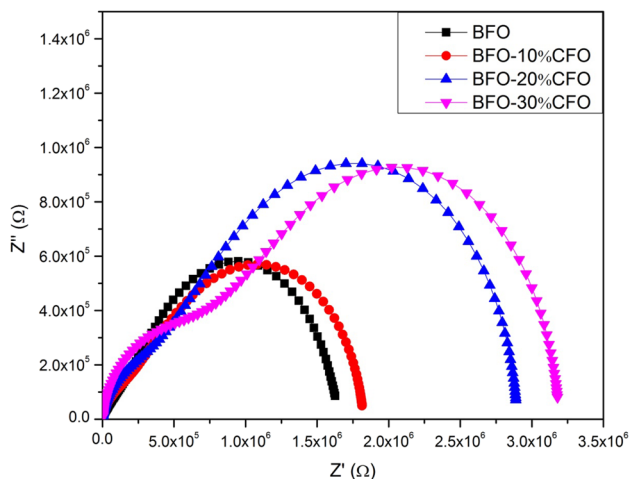
Fig. 12 Nyquist (Cole–Cole) plots for BFO and BFO–CFO composites at room temperature

References

1. F. Yan, G. Chen, L. Lu, P. Finkel, J. Spanier, Appl. Phys. Lett. **88**, 212907 (2013)
2. M. Fiebig, T. Lottermoser, D. Meier, M. Trassin, Nat. Rev. Mater. **1**, 16046 (2016)
3. Y. Lin, P. Kang, H. Yang, M. Liu, J. Mater. Sci.: Mater. Electron. **26**, 1102–1106 (2015)
4. W. Eerenstein, N.D. Mathur, J.F. Scott, Nature **442**, 759–765 (2006)
5. M.S. Bernardo, Bol. Soc. Esp. Ceram. Vidr. **53**, 1–14 (2014)
6. L.W. Martin, S.P. Crane, Y.-H. Chu, M.B. Holcomb, M. Huijben, C.-H. Yang, N. Balke, R. Ramesh, J. Phys.: Condens. Matter. **20**, 434220 (2008)
7. A.K. Pradhan, K. Zhang, D. Hunter, J.B. Dadson, G.B. Loutts et al., J. Appl. Phys. **97**, 093903 (2005)
8. X.L. Lu, J.W. Zhang, C.F. Zhang, Y. Hao, RSC Adv. **5**, 58640–58643 (2015)
9. Y. Wang, J. Hu, Y. Lin, C.-W. Nan, NPG Asia Mater. **2**, 61–68 (2010)
10. G. Catalon, J.F. Scott, Adv. Mater. **21**, 2463–2485 (2009)
11. Y. Li, X. Fang, M. Cao, Sci. Rep. **6**, 24837 (2016)
12. Y. Li, W.-Q. Cao, J. Yuan, D. Wang, M.-S. Cao, J. Mater. Chem. C **3**, 9276 (2015)
13. R. Mazumder, P. Sujatha Devi, D. Bhattacharaya, P. Choudhary, A. Sen, M. Raja, Appl. Phys. Lett. **91**, 062510 (2007)
14. S. Goswami, D. Bhattacharaya, C.K. Ghosh, B. Ghosh, S.D. Kaushik, V. Siruguri, P.S.R. Krishna, Sci. Rep. **8**, 3728 (2018)
15. R. Ramesh, N.A. Spaldin, Nat. Mater. **6**, 21–29 (2007)
16. K.G. Yang, Y.L. Zhang, S.H. Yang, B. Wang, J. Appl. Phys. **107**, 124109 (2010)
17. J. Rout, R.N.P. Choudhary, Phys. Lett. A **380**, 288–292 (2016)
18. Y. Li, Z. Wang et al., Nat. Commun. **6**, 6680 (2015)
19. B.P. Jacob, S. Thankachan, S. Xavier, E.M. Mohammed, J. Alloys Compd. **541**, 29–35 (2012)
20. N.B. Velhal, N.D. Patil, A.R. Shelke, N.G. Deshpande, V.R. Puri, AIP Adv. **5**, 097166 (2015)
21. M. Kumar, S. Shankar, O. Parkash, O.P. Thakur, J. Mater. Sci.: Mater. Electron. **25**, 888–896 (2014)
22. C.M. Kanamadi, J.S. Kim, H.K. Yang, B.K. Moon, B.C. Choi, J.H. Jeong, J. Alloys Compd. **481**, 781 (2009)
23. X.-M. Liu, S.-Y. Fu, C.-J. Huang, Mater. Sci. Eng. B **121**, 255–260 (2005)
24. Y. Qu, H. Yang, N. Yang, Y. Fan, H. Zhu, G. Zou, Mater. Lett. **60**, 3548–3552 (2006)
25. Q. Zhu, Y. Xie, J. Zhang, Y. Liu, Q. Zhan, H. Miao, S. Xie, J. Mater. Res. **29**, 657–664 (2014)
26. M. Tyagi, M. Kumari, R. Chatterjee, A.-C. Sun, P. Sharma, IEEE Trans. Magn. **50**, 2500704 (2014)
27. R.K. Mishra, D.K. Pradhan, R.N.P. Chaudhary, A. Banerjee, J. Phys. Condens. Matter **20**, 045218 (2008)
28. Z. Li, Y. Wang, C.-W. Nan, Phys. Rev. B **79**, 180406R (2009)
29. S. Kamba, D. Nuzhnyy, M. Savinov, J. Sebek, J. Petzelt, Phys. Rev. B **75**, 024403 (2007)
30. R. Haumoni, J. Kreisel, P. Bouvier, F. Hippert, Phys. Rev. B **75**, 132101 (2006)
31. N. Adhlakha, K.L. Yadav, R. Singh, J. Mater. Sci. **50**, 2073–2084 (2014)
32. S. Chandarak, M. Unruan, T. Sareein, A. Ngamjarurojana, S. Maensiri, P. Laoratanakul, S. Ananta, R. Yimnirun, J. Magn. **14**, 120–123 (2009)
33. M.M. Kumar, S. Srinath, G.S. Kumar, S.V. Suryanarayana, J. Magn. Magn. Mater. **188**, 203–212 (1998)
34. V.M. Gaikwad, S.A. Acharya, J. Alloys Compd. **755**, 168–176 (2018)

35. Q. Hang, Z. Xing, X. Zhu, M. Yu, Y. Song, J. Zhu, Z. Liu, J. Ceram. Int. **38**, S411–S414 (2012)
36. P. Kumar, M. Kar, J. Alloys Compd. **584**, 566–572 (2014)
37. D.S. Kim, C. Cheon, S.S. Lee, J.S. Kim, Appl. Phys. Lett. **109**, 202902 (2016)
38. B.K. Bammannavar, L.R. Naik, B.K. Chougule, J. Appl. Phys. **104**, 064123 (2008)
39. S. Jabez, S. Mahalakshmi, S. Nithiyanantham, J. Mater. Sci.: Mater. Electron. **28**, 5504–5511 (2016)
40. P. Uniyal, K.L. Yadav, J. Phys.: Condens. Matter. **21**, 012205 (2009)
41. M. Kumar, S. Shankar, R.K. Kotnala, O. Parkash, J. Alloys Compd. **577**, 222–227 (2013)